Thermal effect on microstructure and mechanical properties in directed energy deposition of AISI 316L

Liu, Weiwei; Hu, Guangda; Yan, Zhaorui; Liu, Bingjun; Wang, Tandong; Lyu, Zhenxin

DOI
10.1007/s00170-024-14274-4

Publication date
2024

Document Version
Final published version

Published in
International Journal of Advanced Manufacturing Technology

Citation (APA)
Liu, W., Hu, G., Yan, Z., Liu, B., Wang, T., & Lyu, Z. (2024). Thermal effect on microstructure and mechanical properties in directed energy deposition of AISI 316L. *International Journal of Advanced Manufacturing Technology*, *134*(7-8), 3337-3353. https://doi.org/10.1007/s00170-024-14274-4

The International Journal of Advanced Manufacturing Technology
https://doi.org/10.1007/s00170-024-14274-4

ORIGINAL ARTICLE

Thermal effect on microstructure and mechanical properties in directed energy deposition of AISI 316L

Weiwei Liu[1,2,3] · Guangda Hu[1,2] · Zhaorui Yan[4] · Bingjun Liu[1,2] · Tandong Wang[1,2] · Zhenxin Lyu[1,2]

Received: 29 August 2023 / Accepted: 12 August 2024

Abstract
At present, in the directed energy deposition (DED) of metals, the heat transfer of the melt pool and microstructural evolution are not fully understood. This study investigates the thermal effect on the microstructure and the mechanical properties of DED AISI 316L, using in situ optical monitoring. Five thin-wall samples were tested to determine the effect on microstructural evolution and mechanical properties with variable laser powers and scanning speeds. A comprehensive optical monitoring system with a CMOS (coaxial complementary metal oxide semiconductor) visual module and an infrared camera was adopted in analyzing the temperature gradient and the solidification rate. The emissivity of the melt pool was calibrated, using the melt pool length, extracted from the coaxial visual image. The results showed that microstructures mainly consist of the coarse columnar grain and the equiaxed grain at the top layer of AISI 316L samples. The direction of epitaxial growth of columnar grains is affected by the compromise between directional heat flux and crystallographic direction. High numerical temperature gradient and high solidification rate are beneficial to obtaining fine grain size and high yield stress. A modified microstructure map for DED AISI316L was established, which correlates the solidification parameters with a solidification microstructure. This research study, combining temperature distribution, solidification parameter, microstructure, and tensile property, provides an experimental identification of solidification parameters and the model on the solidification theory for precision control of DED process.

Keywords Directed energy deposition · Thermal monitoring · AISI 316L · Microstructure

1 Introduction

Directed energy deposition (DED) is a layer-by-layer additive manufacturing technology that generates a molten pool by a laser beam and relies on carrier gas to transport the powder to the molten pool to melt and solidify in the molten pool [1]. DED is not only applied to coatings, but also widely used in large-scale structure manufacturing. At the same time, due to the ability of DED to manufacture complex geometric parts with near net shape, and the possibility of producing integral metal and functionally graded parts, it has a unique position in the additive manufacturing process [2, 3]. In addition, DED has a wide range of applications in biomedicine and aerospace [4, 5]. However, the influence of DED process settings (mainly the laser power, scanning speed, and hatching space of the process) on the microstructure and mechanical properties of the deposited material and the underlying thermal transfer mechanism are still not fully understood. The study of in situ thermal monitoring and the microstructural evolution is one of the research concerns in the realm of metal additive manufacturing.

Many studies have explored various devices and measuring techniques to in situ monitor the thermal behaviors of the melt pool during AM processes. Chen et al. [6] developed a coaxial visual sensing system based on laser

✉ Weiwei Liu
liuww@dlut.edu.cn

1 School of Mechanical Engineering, Dalian University of Technology, Dalian 116024, China

2 State Key Laboratory of High-Performance Precision Manufacturing, Dalian University of Technology, Dalian 116024, China

3 Ningbo Institute of Dalian University of Technology, Ningbo 315000, China

4 Faculty of Mechanical, Maritime and Materials, Delft University of Technology, Mekelweg 2, 2628 Delft, CD, Netherlands

Published online: 30 August 2024

direct metal deposition and investigated the evolution of the molten pool during single-trace-single-layer and single-trace-multi-layers experiments. Zheng et al. [7] found that the microstructure evolution is complex due to the presence of high thermal gradients and dynamic flows in a fast-moving melt pool with associated rapid solidification and layer-by-layer deposition. Hu et al. [8] analyzed the microstructure of CoCrMo alloy prepared by laser melting deposition (LMD) under different powers. It was found that with the increase of laser power, the sizes of equiaxed grain and columnar grain in different regions increase, but the increasing trend is relatively gentle. Hooper [9] developed a coaxial image system to monitor the melt pool dynamics and a temperature range between 1000 and 4000 K was measured. Nedjed et al. [10] found that the cooling rate has an effect on the microstructure. Farshidianfar et al. [11] used a closed-loop control system based on infrared thermal imager to control the microstructure by adjusting the travel speed and controlling the cooling rate in real time. Criales et al. [12] developed a paraxial IR thermal monitor system for the laser powder bed fusion process. This system was applied to measure the melt pool temperature and powder spattering. Misra et al. [13] used the thermal characteristics captured by the infrared pyrometer to analyze various thermal characteristics and found out their relationship with the evolved microstructure, degree of substrate dilution, deposit dimensions, phase formation, and microhardness. Kriczky et al. [14] extracted the temperature gradient, melt pool size, and the temperature from the coaxial thermal image, and compared these thermal characteristics with those in the different areas of the parts. The recent developments of in situ thermal monitoring mainly focused on IR monitoring techniques due to the harsh experimental conditions. Emissivity is a key variable for obtaining accurate temperature signals, so it is crucial for studying the internal stress and microstructure formation of additive manufacturing parts [15]. Farshidianfar et al. [16] in their research set this variable constant by ignoring its influence on cooling rate. Marshall et al. [17] conducted high-temperature calibration using temperature signals from a dual-wavelength pyrometer. Doubenskaia et al. [18] determined the emissivity by distinguishing the solid–liquid phase transition at known temperatures. Devesse et al. [19] calibrated the emissivity of the melt pool using a hyperspectral line camera and temperature was deduced from the spectra at a different wavelength. Emissivity is a dynamic variable, varying with the unstable melt pool surface and the melt pool temperature. Furthermore, model-based calibration of emissivity demands accurate mathematical models and mass data, which makes the calibration process time-consuming for in situ monitoring and control. Therefore, considering the dynamics of melt pool with different process settings, a careful and effective calibration of emissivity is necessary.

Many studies have reported the progress on the DED process parameters optimization, microstructure, and mechanical properties of laser-based additive manufacturing of AISI 316L. Yang et al. [20] investigated the effects of the pulsed laser and continuous laser on the corrosion resistance and microstructure of the sample, with lower pulse frequencies contributing to the formation of finer equiaxial dendrites. Saboori et al. [21] carried out a comparative study on the microstructure and mechanical properties of DED of AISI 316L. The results show that the lower cooling rate and undercooling in DED process is more suitable for large grain size and growth of columnar grain. Akbari et al. [22] reported that the shorter the time interval between layers of thin-walled alloys of AISI316L parts, the slower the cooling rate and the coarser the grain size. The microstructure of as-deposited AISI 316L consists of austenitic and delta ferrite in the inter-dendrite spaces [23]. Roehling et al. [24] studied the laser intensity profile ellipticity for microstructure variation and found that the microstructure can be controlled by a designed-varying laser intensity profile. Terrassa et al. [25] improved the compressive yield stress and density of DED AISI 316L parts by hatch rotation angle. Preferred grain orientation and grain elongation increase are achieved due to the consistent direction of heat flow by parallel-hatching scanning pattern. Generally, the various solidification structure, grain size, and microstructure texture result in different and anisotropic mechanical properties [26].

Understanding the thermal behaviors and solidification is significant to achieving the expected microstructure and mechanical properties. The solidification microstructure was mainly characterized by the grain size, microstructure morphology (planar, cellular, columnar dendritic and equiaxed dendritic), and the solidification texture. Theory on solidification has provided solidification parameters for analyzing and controlling these resultant microstructure characteristics [27, 28]. Kurz and Fisher [29] derived the primary dendrite arm spacing (PDAS) as the function of temperature gradient and solidification rate based on the Müller-Krumbhaar stability criterion. Huang et al. [30] developed a rapid prediction model of thermal characteristics and solidification parameters for DED AISI 316L and Inconel 625. The calculated thermal characteristics were used to predict PDAS and second dendrite arm spacing at different process parameters. Raghavan et al. [31] proposed a localized scanning strategy to control the grain size of Inconel 625 and the predicted PDAS agrees well with experimental results. Bertoli et al. [32] predicted the temperature gradient, solidification rate, and cooling rate based on Rosenthal's solution. Gäumann et al. [33] proposed a microstructure selection map to predict columnar to equiaxed transition (CET) in the deposition

process based on Hunt's model. This model was obtained also by considering the local temperature gradient and solidification rate. Ren et al. [34] modified microstructure selection map, considering the cooling rate and microstructure characterization for laser solid forming of Ti-6Al4V. Akbari et al. [22] extracted the cooling rate from the coaxial visual image of the melt pool and correlated the cooling rate to the tensile properties of AISI 316LSi components. Yin et al. [35] studied the heat flux orientation and grain texture during the SLM process, using a numerical model. The maximum heat flow direction turned to the building direction at a high laser power and high scanning speed.

Overall, the thermal behaviors of the melt pool can be monitored using IR techniques, which can be applied to explain the microstructural evolution guided by solidification theory. The microstructures are mainly determined by solidification parameters: undercooling, temperature gradient, and solidification rate. However, there is a gap between the fundamental solidification theories and the monitoring that these solidification parameters estimated by time-expensive numerical methods are not practical for real-time analysis of the microstructure and properties in the online DED process. An experimentally decided microstructure map with measured temperature gradient and solidification rate, which can provide with controllable process signals for control of solidification microstructures in a DED process has not been widely reported. Therefore, it is a crucial study to determine these solidification parameters through a collection of laboratory experimental data, and the aim is to reveal the valuable relationships of solidification parameters, the microstructure, and mechanical properties in DED process.

In this study, a comprehensive optical monitoring system, with a coaxial CMOS module and an IR camera, was set up to monitor the thermal behavior during the DED process of AISI 316L. The high-temperature emissivity was calibrated using the melt pool length in visual images. Five thin-wall samples were fabricated by DED to analyze the solidification microstructure and the mechanical properties of the samples. The solidification parameters extracted from temperature distribution were used in in situ analysis of microstructure and the sample mechanical properties.

In the rest of this paper, "Sect. 2" introduces the design of experiments, characterization methods of deposition material, and "Sect. 3" is about emissivity calibration and the extraction of solidification parameters. "Sects. 4" and "5" discuss the results and the framework linking the parameters, microstructure, and properties. And the paper ends in "Sect. 6" of the conclusions.

2 Experimental design

2.1 DED process and the monitoring system

Five thin-wall samples (70 mm × 70 mm) of AISI 316L stainless steel were fabricated using directed energy deposition system as shown in Fig. 1. The DED system consists of a diode laser generator (LDF 4000–100 VGP, Laserline GmbH), a six-axis robot (KR30HA, KUKA Roboter GmbH), a laser head (YC52, Precitec KG), and a metal powder feeder (RC-PF-01B-2, Raycham Ltd). The initial defocusing distance of 14 mm (negative defocusing) was chosen to enhance the stability of the deposition process and a laser beam diameter of around 2 mm was generated at this distance. A liquid melt pool was produced and AISI 316L powder was injected into the melt pool by the carrier gas. Argon (purity 99.999%) was used for both carrier gas and shielding gas. Commercial AISI 316L powder (Höganäs) with a diameter of 45–150 µm was deposited on AISI 316L substrate. The chemical composition of the AISI 316L powder is shown in Table 1. The laser head stays at the beginning and the end of each path to prevent the edge collapse. The interval time between each layer is 10 s. Laser power and scanning speed are two main parameter settings of the

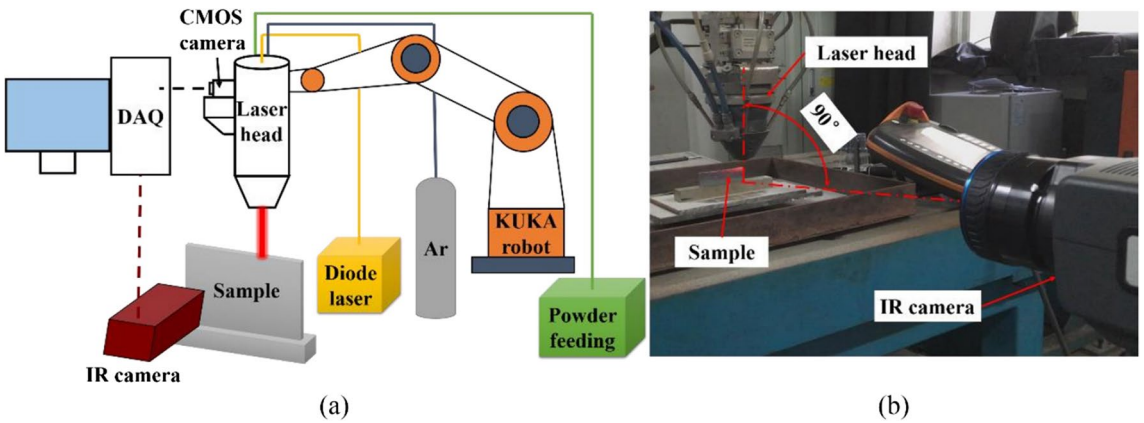

Fig. 1 Schematic of experimental setups (**a**) and the monitoring conditions (**b**)

Table 1 Chemical compositions of AISI 316L powder (wt.%)

Elements	C	Mn	N	Mo	Cr	Si	Fe
wt.%	0.022	1.6	12.5	2.5	17.0	0.7	Bal

process, influencing the microstructure and mechanical properties of deposited AISI 316L in DED. The main parameters studied in this paper are listed in Table 2. The variation of *Z*-step was decided to avoid geometry collapse based on the height of the deposition layer in the single-track study.

A medium-wave infrared camera (FLIR Systems, Inc) with the spatial resolution of 640 × 512 and a temperature range of 500–2000°C was used to paraxial monitor the temperature distribution of the melt pool and the thin-wall samples. A CMOS module (MQ013MG-ON, XIMEA) with the acquisition resolution of 1.3 Mptx and maximum acquisition rate of 172 fps is integrated into the DED system for in situ melt pool image acquisition and extraction of the melt pool length.

In the design of experiment, five single-path, thin-wall samples were designed and fabricated for both paraxial thermal monitoring of DED process and the sample tensile test. Process parameters (laser power, scanning speed, and *Z*-step) are pre-decided in preliminary experiments for possessing stable geometry and mechanical properties. A single parameter (laser power or scanning speed) was varied to analyze the influence factor on thermal behaviors of the melt pool and resultant properties of the deposition layers. Laser power was selected in different levels for samples 1, 2, and 3, while scanning speed was different for samples 2, 4, and 5. The thermal camera was operating with the focus plane coinciding with the sample to capture the whole temperature distribution and calculate key solidification parameters of the samples. Visual melt pool geometry was extracted from images captured by coaxial CMOS module to calibrate the emissivity of IR camera.

2.2 Characterization

Microstructure analysis was carried out using an optical microscope (NIKON MA 100) and the electron back scattered diffraction (EBSD) technique in a field emission scanning electron microscopy (Zeiss SUPRA 55). An ultra-depth of field microscopic system (KEYENCE VHX 600E) is used to characterize the morphology transition in the top layer of samples. The samples were cut from the area near the tensile fracture and the top layer of the thin-wall samples, using wire-electrode-cutting machining. All five samples were grounded on abrasive paper and polished with the diamond compound before they were etched with aqua regia. The primary arm spacing λ_1 was measured on the transverse surface of the samples in accordance with the standard GB/T 14999.7–2010. Average λ_1 was estimated by calculating the number of grains in the area of the field in view.

The samples for tensile test were cut from thin-wall samples using wire-electrode cutting and machined into samples with a gauge length of 31 mm, gauge width of 10 mm, and the thickness of 2 mm in accordance with GB/T228.1–2010. Tensile tests were performed to evaluate the tensile properties of samples at room temperature with the loading speed of 5 mm/s. The Vickers microhardness testers (MVC-1000B) were used to measure the Vickers microhardness in accordance with GB/T 4340.1–2009. The Vickers microhardness value of each sample was obtained by an averaging value of six spots with a sampling interval of 0.4 mm.

3 Calibration and extraction of solidification parameters

3.1 Calibration of emissivity

Emissivity is the main variable that influences the accuracy of IR measure. In this study, the emissivity was calibrated based on the visual melt pool length. The dimensions of each pixel in the visual image and IR image were first reconstructed. The threshold segmentation was applied to extract the melt pool from the visual image. An enclosing rectangle was employed to acquire the melt pool length as shown in Fig. 2. According to the boundary extraction algorithm, the outer rectangle of the molten pool is made, and the length

Table 2 Parameters and emissivity used in DED of five thin-wall samples

Sample	Laser power (W)	Scanning speed (mm/s)	*Z*-step (mm)	Powder feeding rate (g/min)	Emissivity
1	1000	6	0.4	9.15	0.62
2	1400	6	0.4	9.15	0.67
3	1800	6	0.4	9.15	0.73
4	1400	4	0.5	9.15	0.73
5	1400	8	0.3	9.15	0.64

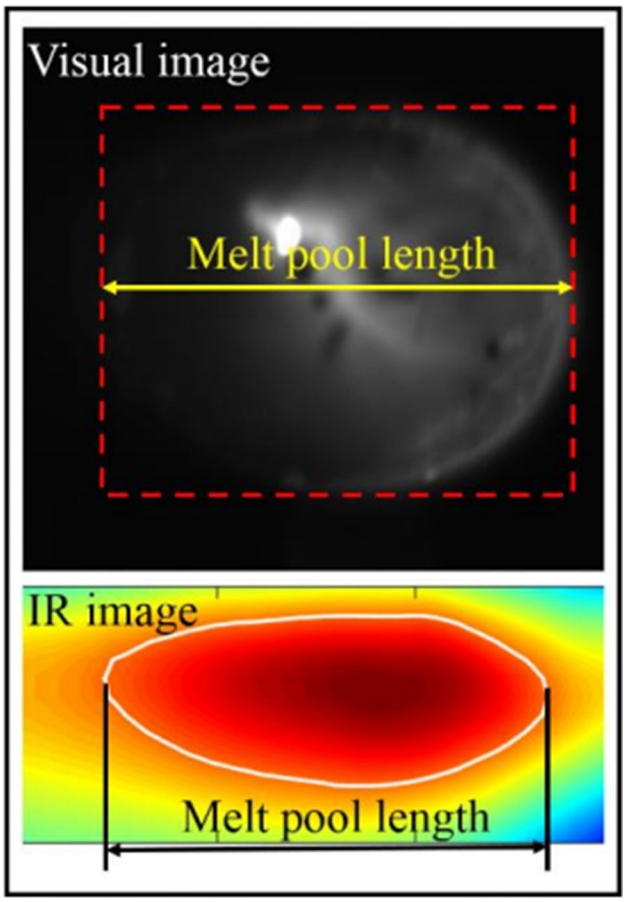

Fig. 2 Emissivity calibration based on the visual melt pool length

of the rectangle is measured to get the length of the molten pool. According to the melting point of the material, the range of the molten pool in the infrared thermal imager is extracted and the length of the molten pool is calculated. The emissivity ε of the infrared thermal imager is adjusted so that the length of the molten pool is equal to the length of the molten pool extracted from the visual image. Different emissivity was determined for the five samples to ensure the precision in data monitoring and acquisition. The estimated emissivity for all samples is listed in Table 2. Higher emissivity was used for the case of larger heat input with a higher temperature. The results that show elevated emissivity at a higher temperature for AISI 316L were observed as well by the study of the reference [36].

3.2 Extraction algorithm for solidification parameters

Guided by metal solidification theory, grain size, growth orientation, and grain structure are mainly controlled by two solidification parameters: temperature gradient G and solidification rate R. Temperature gradient G is defined as the tangent of the temperature distribution with respect to distance. The numerical temperature gradient is given by Eq. (1):

$$G = \nabla \mathrm{T}(x,z) = \frac{\partial T}{\partial x}\vec{i} + \frac{\partial T}{\partial z}\vec{j} \approx G_x\vec{i} + G_z\vec{j} \tag{1}$$

According to Fourier's law, the heat flux can be expressed as following:

$$J_T = -k\nabla \mathrm{T}(x,z) \tag{2}$$

Solidification rate is defined as the moving speed of the solidification interface at the tail of the melt pool. It is difficult to capture a stable and consistent solidification interface because of the evolution of the melt pool during the deposition process.

Simplification of the solidification rate is given by Blecher et al. [37]:

$$R = V\cos\alpha \tag{3}$$

where V is the welding speed, α is the angle between G and x direction, α can be given as follows:

$$\cos\alpha = -\frac{\partial T}{\partial x} / \|\nabla \mathrm{T}(x,z)\| \tag{4}$$

The program framework in Matlab for instantaneous G_t and R_t of DED process is illustrated in Fig. 3. The online temperature data was imported into the G-R program routine. A subroutine was developed to judge if a liquid melt pool was created and the scanning direction of the laser head. Then, the melting point of AISI 316L was used to extract the melt pool elements from the temperature matrix of the thin wall. The temperature gradient G, solidification rate R, and α at time t can be then calculated accordingly.

4 Results

The DED AISI 316L thin-wall sample 1 of 70 × 70 mm is shown in Fig. 4a. The temperature distribution of sample 1 is shown in Fig. 4b. The sample was locally heated and melted by high-power laser irradiation and a new layer was deposited on the previous layers as the laser head scanned along the path. Maximum temperature can be found in the deposition area and the temperature decreased rapidly along the building direction due to the heat sink effect. The floating area is the captured laser head moving above the thin-wall sample. The corresponding temperature distribution of the deposition area in Fig. 4b is shown in Fig. 4c. This temperature distribution well corresponds to the theoretic distribution generated by a moving Gaussian model in the vertical plane. The melting point isotherm of 1670 K is highlighted in white to reveal the liquid melt pool generated by laser irradiation [38].

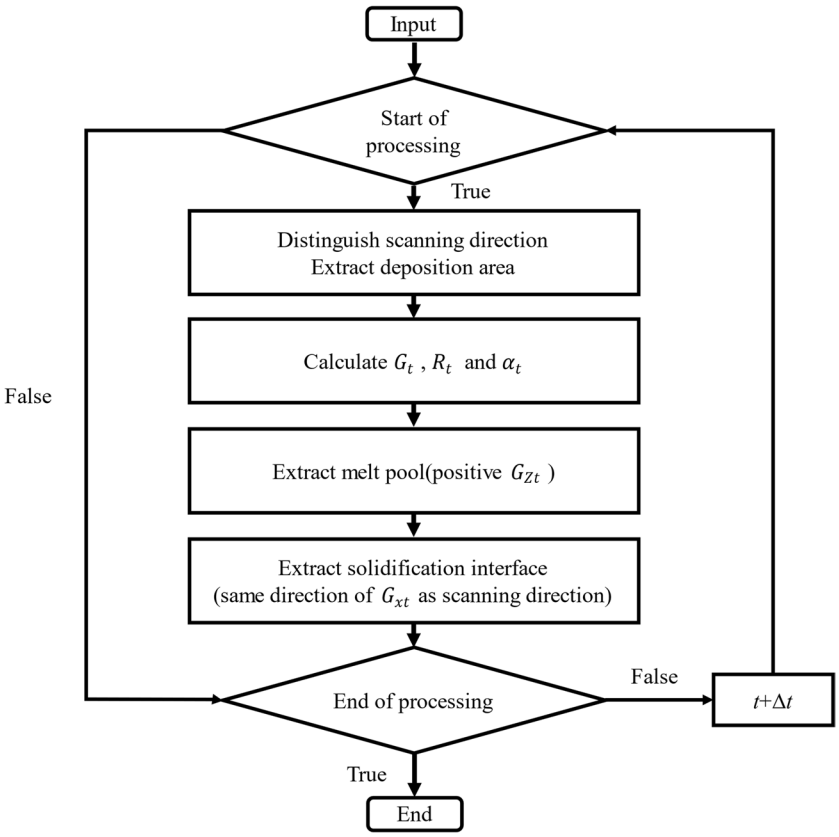

Fig. 3 An algorithm framework for extraction of solidification parameters of G_t, R_t, and α_t

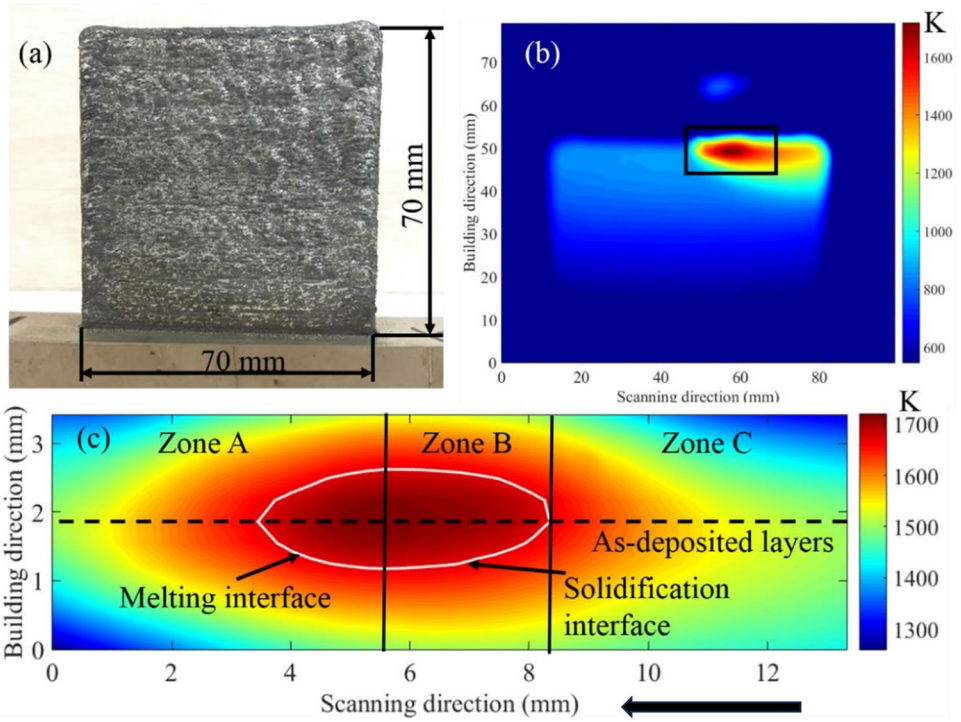

Fig. 4 AISI 316L sample (**a**), temperature distribution (**b**), and identification of melt pool (**c**)

316L powder was heated by laser irradiation in the laser-powder interaction zone above the melt pool. The dynamic solid–liquid interface consists of the consecutive melting interface and solidification interface. The interface can be distinguished based on the temperature gradient direction. Three zones of temperature distribution can be depicted as follows. (A) The heating area of material is characterized by a rapid temperature increase to the maximum temperature of the melt pool and the solid–liquid phase transition at the melting interface. (B) The rapid cooling area of the liquid phase is characterized by a temperature decrease in the melt pool and the liquid–solid phase transition in the solidification interface. (C) The cooling area of solid deposition layer. In zone C, the solid metal experiences temperature decreases due to the heat sink effect of deposition layers.

4.1 Thermal transfer and solidification parameters analysis

4.1.1 Temperature gradient of the melt pool

The temperature gradient of the melt pool has a significant influence on the liquid convection, solidification mode, and grain size. The temperature gradient vector field of the melt pool depicted on the temperature grayscale map at the beginning, middle, and end of one path of the 20th layer of sample 2 is illustrated in Fig. 5a, b, and c, and the corresponding geometries of the thin-walls were shown in Fig. 5d, e, and f. The melt pool turned stable as the laser scanned to the middle of the layer as shown in Fig. 5b. The stability of the melt pool means the temperature distribution and geometry of the melt pool are similar to the theoretical model generated by moving a Gaussian heat source under similar heat input and heat dissipation conditions. The melt pool collapse was captured at two edges of a layer. At the beginning of a layer (Fig. 5a), an unstable melt pool with a deep and short tail was generated by laser irradiating for 0.5 s. The lower height of the edge and the stay time of 0.5 s of laser make the liquid melt pool lack of support of solid metal. Under the influence of gravity, the tail of melt pool collapses at the edge so the local geometry of deposition layer becomes wide and low.

High numerical temperature gradient at the tail of the melt pool was caused by the air dissipation with the gradient direction nearly horizontally pointing to the center. The head of the melt pool was prolonged as the laser head started to move. Similar edge collapse to the head of melt pool collapse at the edge was shown at the end of the deposition layer in Fig. 5c. The melt pool collapse and its influence on

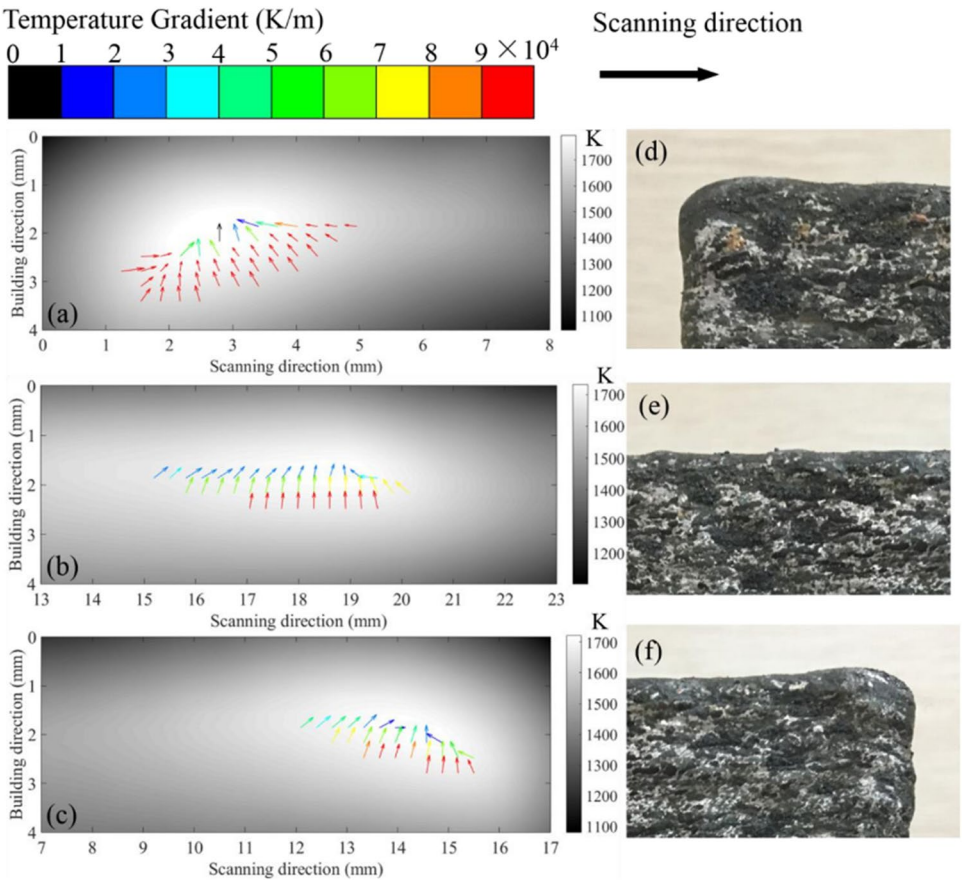

Fig. 5 Numerical temperature gradient of the melt pool at the beginning, middle, and end of one layer

IR temperature signal due to heat accumulation and edge geometry (Fig. 5d and f) were also reported by the reference [39]. Comparing to the complex heat transfer at the edge, temperature gradient direction in the stable state pointed upward rather than the center due to rapid heat conduction downward to the substrate. Different heat dissipation along the deposition layer changed the shape of the melt pool and direction of temperature gradient.

4.1.2 The effect of process parameters on solidification parameters

The effect of laser power and scanning speed on the numerical temperature gradient of the melt pool is shown in Fig. 6. The estimation of temperature gradient at the solid–liquid interface is in the order of 10^5 K/m. The temperature gradient evidently decreased as the laser power increase from 1000 to 1800 W at a constant scanning speed (samples 1, 2, and 3). With the scanning speed increasing from 4 to 8 mm/s, the temperature gradient showed a distribution pattern generated by moving the Gaussian heat source, but the melt pool shrink by comparing samples 4, 2, and 5. The numerical temperature gradient in the melt pool center was less than 4×10^4 K/m and the maximum temperature gradient lied in the solid–liquid interface because of the high heat conduction from the melt pool to the as-deposited layers.

The solidification (the nucleation and growth of grains) is largely governed by the numerical temperature gradient G and solidification rate R at the solidification interface. The effect of laser power on temperature gradient G and solidification rate R along the solidification interface is shown in Fig. 7. The numerical temperature gradient decreased from about 10^5 K/m to 5×10^4 K/m when the laser power increase from 1000 to 1800 W (Fig. 7a). To reduce contingency of monitoring results that are influenced by melt pool movement, the mean and standard deviation of temperature gradient at the solidification interface at different times were calculated to show the overall trend of a layer.

The solidification rate showed a similar trend at different laser power. Solidification rate at the bottom of the melt pool was relatively small and increased along the solidification interface due to the enhanced heat dissipation to the environment and solidified metal (Fig. 7b). The solidification rate difference in the melt pool was also studied in the reference [40], in which it was calculated by a numerical model.

The effect of scanning speed on temperature gradient G and solidification rate R is shown in Fig. 8. The decreasing magnitude of temperature gradient along the solidification interface is more significant at high scanning speed but the mean temperature gradient showed only a little change (Fig. 8a). The solidification rate increased with the scanning speed since the liquid melt pool moved faster with the laser (Fig. 8b). In the previous studies, the influence of scanning speed on the cooling rate and the microstructural evolution was reported in detail, but the role of laser power in solidification parameters of the melt pool was not fully understood

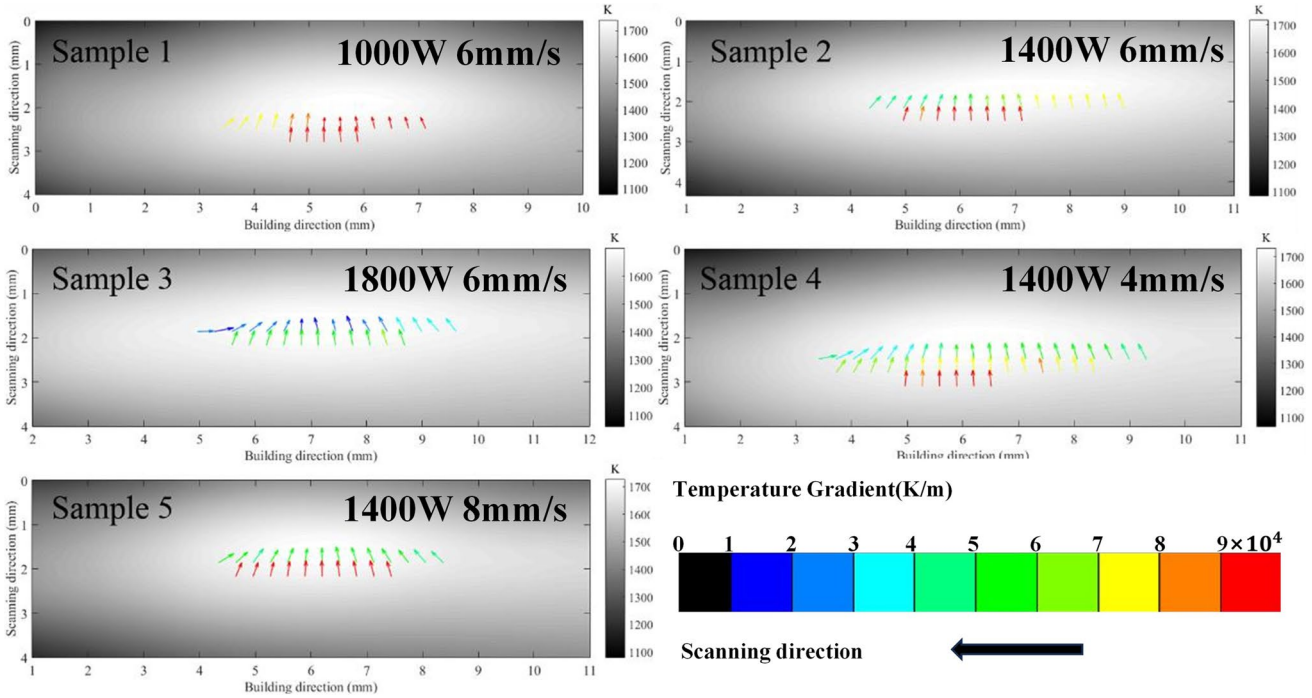

Fig. 6 Effect of laser power and scanning speed on numerical temperature gradient

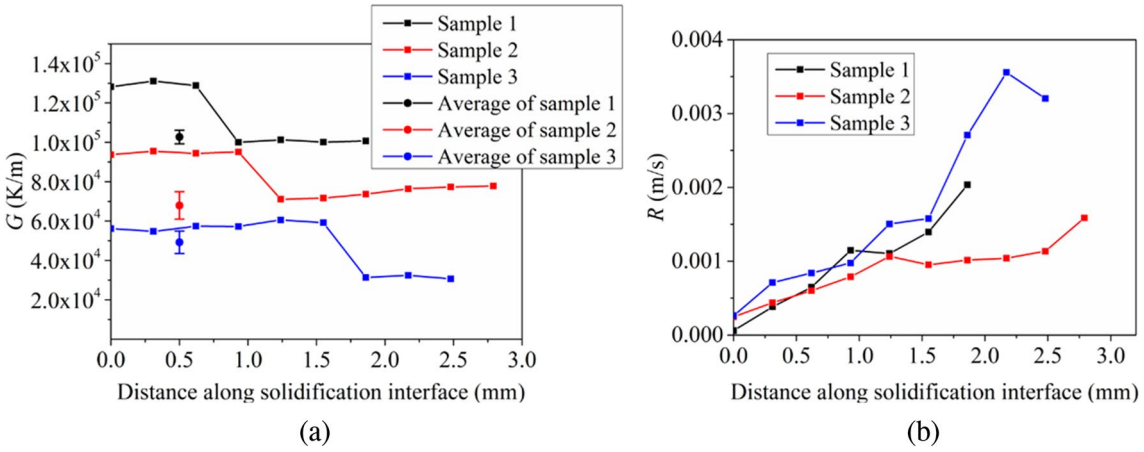

Fig. 7 Effect of laser power on numerical temperature gradient and solidification rate at the solidification interface

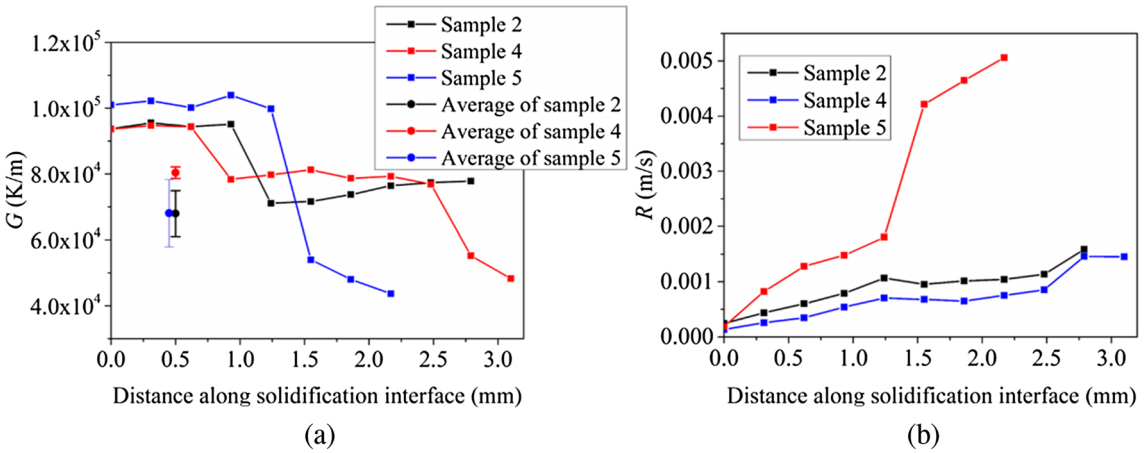

Fig. 8 Effect of scanning speed on numerical temperature gradient and solidification rate

[16]. Considering the joint effect of laser power and scanning speed, the temperature gradient in the solidification interface was largely influenced by laser power from this study (Figs. 7a and 8a above) and the cooling rate is mainly regulated by scanning speed [41].

4.2 Microstructure

The microstructure of DED AISI 316L in sample 2 is shown in Fig. 9. The microstructure consists of coarse columnar grains in the central region and equiaxed grain at the top of the sample (Fig. 9a). Continuous epitaxial growth of columnar grains along build direction is the dominating growth mechanism, noting that most of the columnar grains grew following the orientation of columnar grains in the previous layer (Fig. 9b). EBSD also illustrates that coarse columnar grains exist in two consecutive layers and grows aligning with the building direction (BD). CET occurred at the top of the sample (Fig. 9c). In fact, the melt pool of each layer has a similar heat transfer and solidification condition, so it is reasonable to believe that the growth of columnar grains was stopped by the equiaxed grains in each layer. During the deposition process, a new layer was deposited on previous deposition layers, so the upper part of the deposition layer experienced the processes of re-melting and re-solidification. The remelting band is illustrated in Fig. 9b. The grains grow continuously from the existing columnar grains without requiring nucleation of new grains [26].

The transversal surfaces of the cellular-substructure inside the coarse columnar grains of five samples were compared in Fig. 10. Colonies of this cellular substructure belong to the same coarse columnar grains, which share the same crystallographic direction and similar size. Quantitative characterization of the primary arm spacing λ_1 was conducted following GB/T 14999.7–2010. The basic idea of this estimation method is counting the grain number in the field of view (FOV) and then calculating λ_1 [42]. The results of λ_1 are summarized in Table 3. The results show

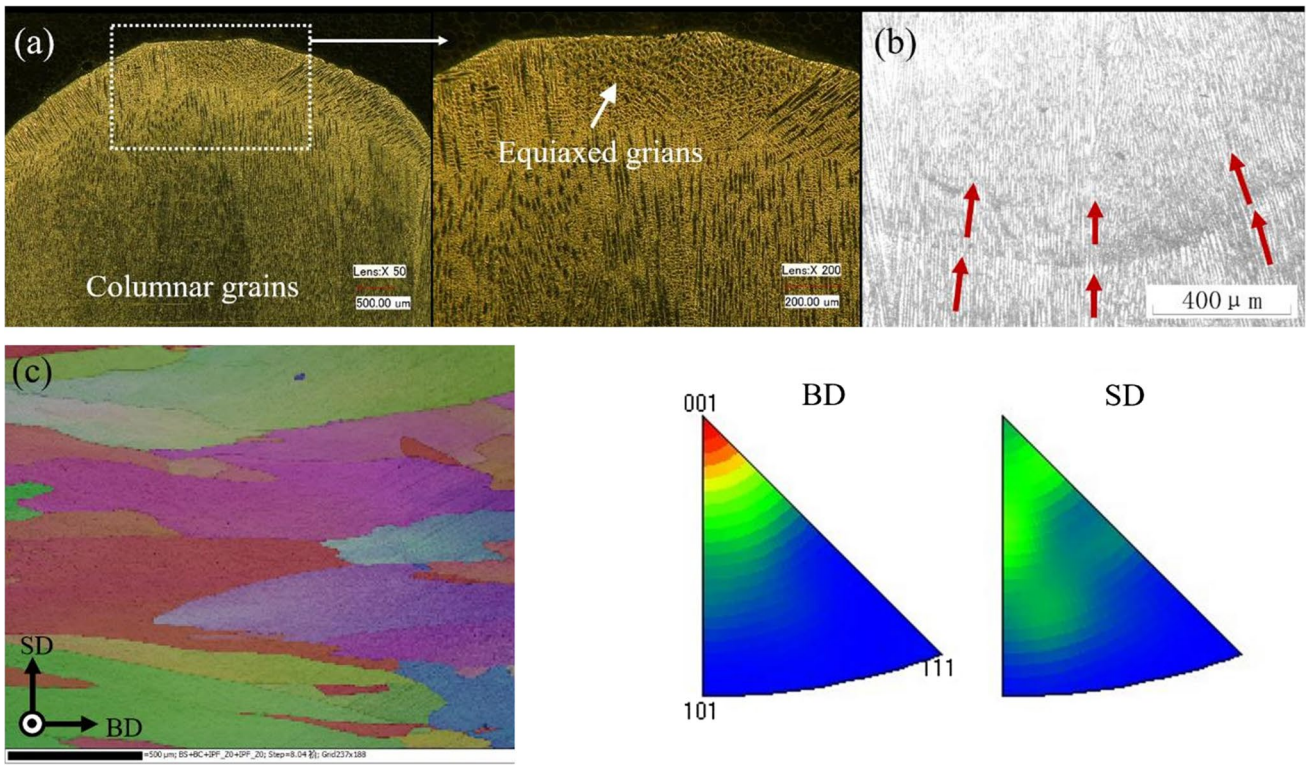

Fig. 9 Microstructures at the top layers (**a**), continuous growth of columnar grains (monitoring plane) (**b**), and EBSD texture plot (**c**)

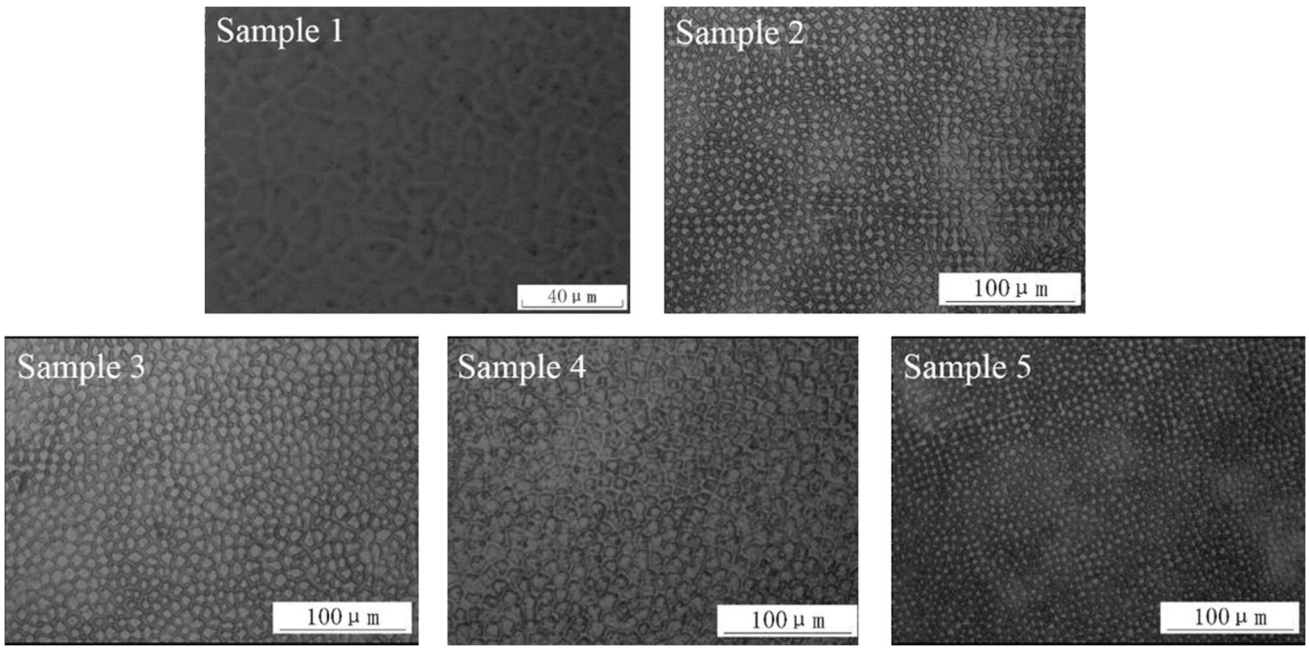

Fig. 10 Comparison of cross-section columnar grains of DED AISI 316L samples

Table 3 Estimation of average λ_1 (primary dendrite arm spacing) of in the middle of AISI 316L samples

Sample	Area of FOV (mm^2)	Grain number in FOV	λ_1(μm)
1	0.003072	146	5.237
2	0.0192	417	7.746
3	0.0192	112	10.299
4	0.0192	320	8.643
5	0.0192	180	6.786

that λ_1 increased from 5.237 to 10.299 μm with the increase of laser power. Comparing the results of samples 4, 2, and 5, λ_1 decreased from 8.463 to 6.786 μm with the increase of scanning speed.

The decrease of λ_1 mainly attributes to the increase of the effective energy input (P/V).

4.3 Mechanical properties

To evaluate the effect of grain size on mechanical properties, the tensile mechanical properties and microhardness were studied. The yield stress (σ0.2) and elongation of five DED AISI 316L samples are shown in Fig. 11a. The σ0.2 decreased from 327.58 to 292.16 MPa with the increase of laser power in samples 1, 2, and 3.

Considering samples 4, 2, and 5, the high scanning speed is beneficial for improving the yield stress. The maximum yield stress reached 342.25 MPa in sample 5. The elongation shows an opposite trend of σ0.2 in the DED AISI 316L samples. The fracture morphology of sample 2 is shown in Fig. 11b. The fracture surface with dimples of different sizes and shapes shows that ductile fracture was the fracture mechanism of samples when they were subjected to axial tensile stress.

The Vickers hardness of five DED AISI 316L samples is compared in Fig. 12.

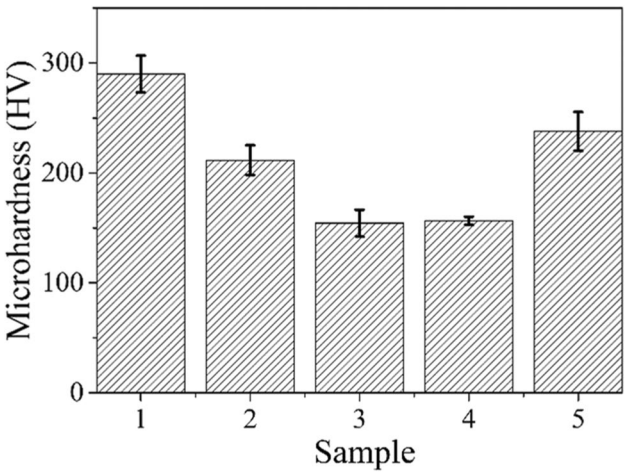

Fig. 12 Microhardness of DED AISI 316L samples

Microhardness of sample 1 is 289.93 HV, which is larger than those of other samples. Vickers hardness decreased to 154.32 HV as the laser power increase to 1800 W in sample 3. Comparing samples 4, 2, and 5, the increase of scanning speed resulted in the hardness increase of DED AISI 316L sample. This increase in Vickers hardness mainly attributed to fine-grain strengthening for the samples.

5 Discussions

5.1 In situanalysis of continuous epitaxial columnar growth

In this study, the zip-zap scanning pattern was used in the deposition but little columnar grains that seriously deviated from building direction have been found. The main growth mechanism is continuous epitaxial growth aligned with the orientation of columnar grains in as-deposited layers (Fig. 9a). For in situ distinguishing the continuous epitaxial

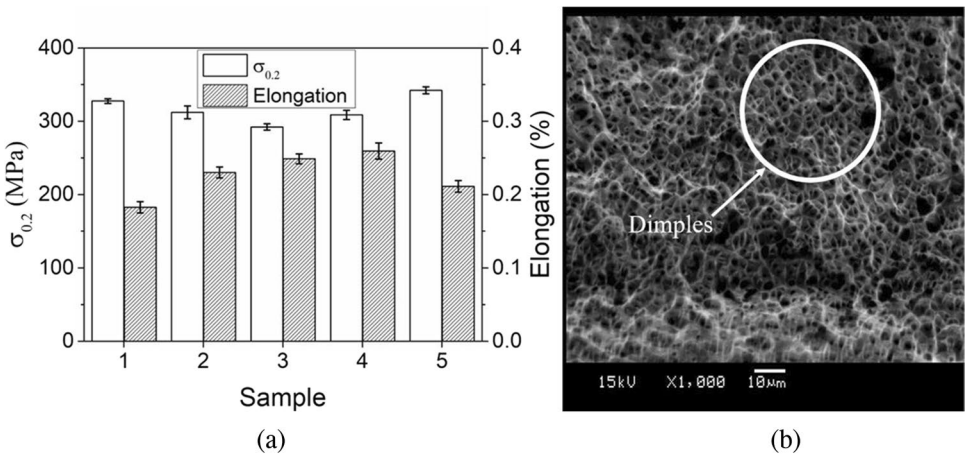

Fig. 11 Tensile mechanical properties of DED AISI 316L samples (**a**) and fracture morphology (**b**)

columnar growth, two solidification problems should be considered: (a) the continuous columnar morphology of grain and (b) the similar growth orientation of columnar grains. The equiaxed grains were melted during depositing the next layer and new columnar grains grew at the solidification interface.

The growth orientation of columnar grains is mainly influenced by directional heat flux and crystallographic direction. Austenite stainless steels are face-centered cubic structure and easy-growth direction is the direction of $<100>$. Under the influence of high numerical temperature gradient, the easy-growth direction of columnar grains grows aligning with the maximum orientation of heat flux. The main orientation of heat flux is between $\pm 30°$ with respect to building direction for consecutive two deposition layers in a bidirectional scanning pattern under similar heat conditions, which agrees well with the growth orientation of columnar grains as shown in Fig. 13. The crystallographic direction of $<100>$ that aligns closely with the maximum heat flow direction at the solid–liquid interface achieved preferred growth during the solidification. The continuous epitaxial columnar growth and the growth direction of columnar grains can be in situ predicted through monitoring of the heat flux direction.

5.2 Prediction of columnar to equiaxed transition

Results (Fig. 9b) show that CET occurred at the upper part of the deposition layer in DED of AISI 316L. The CET occurs when nucleation of sufficiently numerous equiaxed grains takes place in the constitutionally undercooled liquid adjacent to the columnar dendrite front [33], and this process is controlled by the temperature gradient G, solidification rate R, and undercooling. A modified microstructure map based on the Gäumann model [33] was developed by integrating measured solidification parameters to predict the CET of DED AISI 316L. The AISI 316L is simplified as Fe-17Cr-12Ni ternary alloy and each component is considered independently for linear superposition of each component. The constitutional tip undercooling ΔT_c can be expressed as follows:

$$\Delta T_c = m_{\mathrm{Ni}}\left(C_{0,\mathrm{Ni}} - C_{l,\mathrm{Ni}}\right) + m_{\mathrm{Cr}}\left(C_{0,\mathrm{Cr}} - C_{l,\mathrm{Cr}}\right) \tag{5}$$

where m_{Ni} and m_{Cr} are the liquidus slopes of the solute elements Ni and Cr, $C_{0,\mathrm{Ni}}$ and $C_{0,\mathrm{Cr}}$ are the nominal concentrations of the elements Ni and Cr in the alloy, and $C^*_{l,\mathrm{Ni}}$ and $C^*_{l,\mathrm{Cr}}$ are the concentrations of the liquid tip elements Ni and Cr.

The constitutional tip undercooling, ΔT is given approximately by the following:

$$\Delta T = \Delta T_c = (a \bullet R)^{1/n} \tag{6}$$

Gäumann CET model can be given as follows:

$$G = \frac{1}{n+1} \bullet \sqrt[3]{\frac{-4\pi}{3\ln(1-\varnothing)}} \bullet N_0^{1/3} \bullet \left[1 - \frac{\Delta T_n^{n+1}}{(aR)^{(n+1)/n}}\right](aR)^{1/n} \tag{7}$$

where N_0 is the nuclei density, ϕ is the volume fraction of the equiaxed grains, a and n are material-dependent constants. Constants a and n in this study were numerically solved by constitutional tip undercooling ΔT_c equations. For the process window, $n = 2.2$ and $a = 6401$ are calculated. The physical properties of AISI 316L used in this model are listed in Table 4. For DED process with high numerical temperature

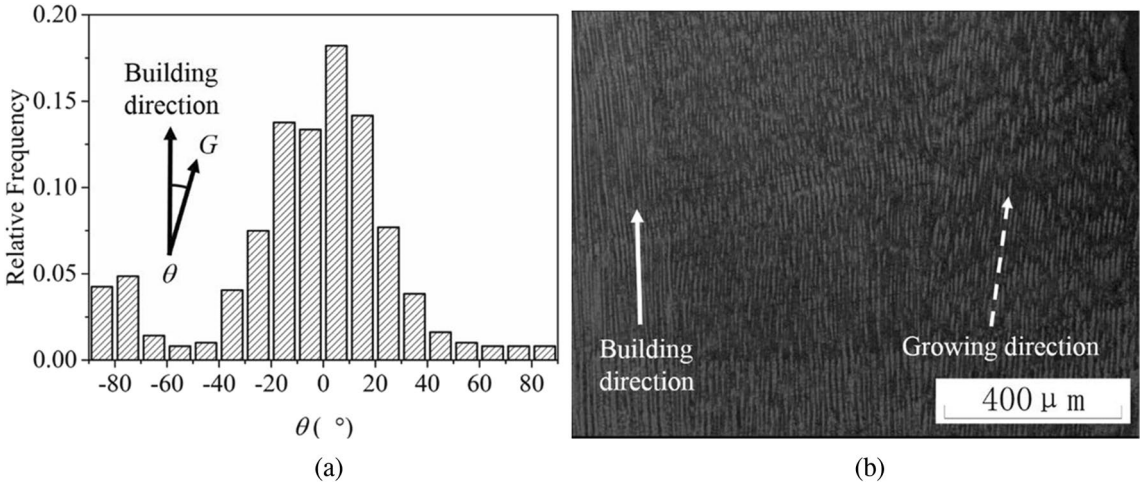

Fig. 13 The orientation of heat flux (**a**) and growing direction of columnar grains (**b**)

Table 4 Physics properties of AISI 316L [33, 43]

Properties	Value
Nuclei density N_0	2×10^{15}
Volume fraction of equiaxed grains ϕ	0.05
Slope of the liquidus surface with respect to chromium concentration m_{Cr}	− 3.00 K/wt.%
Slope of the liquidus surface with respect to nickel concentration m_{Ni}	− 1.08 K/wt.%
Partition coefficient for chromium k_{Cr}	0.89/
Partition coefficient for chromium k_{Ni}	0.98
Gibbs–Thomson coefficient Γ	1.9×10^{-7}Km
Diffusion coefficient for chromium D_{Cr}	2.67×10^{-7}m^2/s
Diffusion coefficient for nickel D_{Ni}	4.92×10^{-7}m^2/s

gradient G, the nuclei density N_0 is significant and ΔT_n can be safely neglected. The relationship can be obtained by the following:

$$\frac{G^n}{R} = a\left\{\sqrt[3]{\frac{-4\pi}{3ln(1-\varnothing)}} \bullet \frac{1}{n+1}\right\} \tag{8}$$

Figure 14 shows the solidification map for columnar to equiaxed transition of AISI 316L with DED parameters window. The solidification parameters for the large fraction of the melt pool were above the CET curve in the columnar zone and solidification parameters at the top of the melt pool are in the equiaxed zone. Columnar structure in the main part of the sample can be derived from high $G^{2.2}/R$ ratio and the CET at the top of the sample (Fig. 9) can be estimated by the low $G^{2.2}/R$ in this modified microstructure map, which provides an experimental tool to in-situ analyze CET during the process.

5.3 Relationship between solidification parameters, λ_1, and mechanical properties

Considering the complexity of parameter effects on the microstructure and properties, it is difficult to directly control the solidification structure and mechanical properties of the DED components. Among the multi-physics coupling with the melt pool during the DED process, temperature distribution can be in situ monitored by IR technique among factors that influence the microstructure and mechanical properties. The local solidification condition mainly influences the grain size. Thus, establishing a relationship among the process settings, solidification parameters, primary arm spacing, and tensile properties is essential. In this paper, the Kurz-Fisher model [29] is used to discuss this thermal-primary arm spacing relationship—the material is simplified as a binary system. The modified equation at high solidification rate between λ_1, experimentally measured G and R can be expressed as follows:

$$\lambda_1 = 4.3k_T\left(\frac{\Delta T_0 D\Gamma}{k}\right)^{1/4} R^{-1/4}G^{-1/2} \tag{9}$$

where ΔT_o is the equilibrium solidification range, D is the diffusion coefficient, k is the partition coefficient, and k_T is the thermal coefficient decided by experiments. The material-dependent properties are listed in Table 4. The numerical temperature gradient of the solidification interface and solidification rate is extracted from the temperature distribution recorded by IR camera. Figure 15 shows the processing map of λ_1 as the function of G and R. The primary arm spacing decreases with a temperature gradient of the solidification interface G and solidification rate R increasing. At the laser power of 1000 W, the high numerical temperature

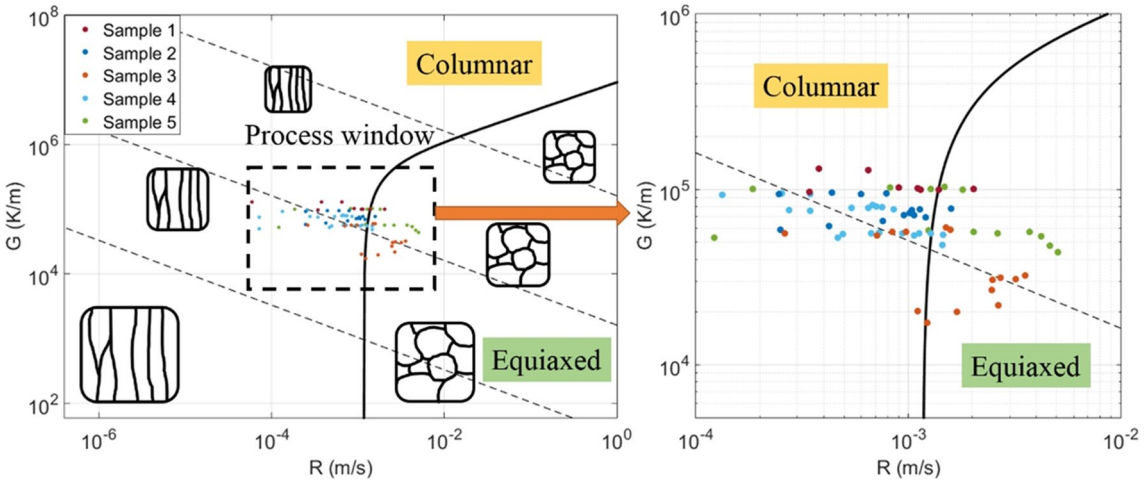

Fig. 14 Effect of solidification parameters on CET of DED AISI 316L

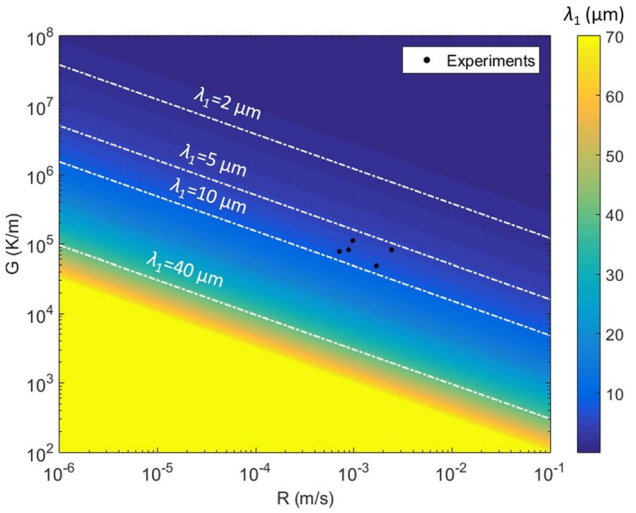

Fig. 15 Relationship between experimentally measured solidification and λ_1 (primary dendrite arm spacing) of cell substructure

gradient of the solidification interface mainly contributed to the grain refinement since solidification rate was relatively kept stable. The effect of scanning speed on the grains size is that the increasing solidification rate with scanning speed resulting in a smaller λ_1. Though scanning speed has played an important role in determining the grain size, the effect of laser power on λ_1 cannot be neglected in experiments since it mainly influences the heat input and temperature gradient.

The mechanical properties of DED metal change with the solidification texture, microstructure morphology, and grain size. No martensitic transformation occurred during the solidification of AISI 316L stainless steel and the sample mainly consists of coarse columnar grains, so the yield stress at room temperature largely depends on the orientation and λ_1 of cell substructure. Only tensile mechanical properties in building direction are considered in this study. The primary arm spacing and yield stress relationship are expressed using the Hall–Petch relationship:

$$\sigma_{0.2} = \sigma_0 + k_\sigma \lambda_1^{-0.5} \tag{10}$$

where σ_0 and k_σ are material-dependent constants. Figure 16 shows the relationship between yield stress and λ_1 of DED AISI 316L. The increase of λ_1 leads to an increase in yield stress. The Hall–Petch coefficient k_σ may change with different grain size and strain ε due to different dislocation density and the propagation of dislocation [44]. But the error of the Hall–Petch relationship in this paper is acceptable considering the small variation of primary arm spacing (from 5.2 to 10.2 μm), and the samples have a similar strain with yield stress. The hardening rate plot of samples 1, 2, and 3 (Fig. 16b) also shows that the samples with different λ_1 share similar Hall–Petch behaviors based on the study between hardening rate and Hall–Petch relationship [45]. The λ_1 also shows the influence on the elongation and Vickers microhardness. The change of elongation and yield stress showed the opposite trend. The decrease of λ_1 leads to the increase of microhardness. Integrating the extracted solidification parameters, Eq. (9), and Hall–Petch relationship, a framework relationship is developed to link the process parameters, thermal behaviors, and microstructure and mechanical properties in DED of AISI 316L. This relationship can provide an experimental and theoretical guide in selecting

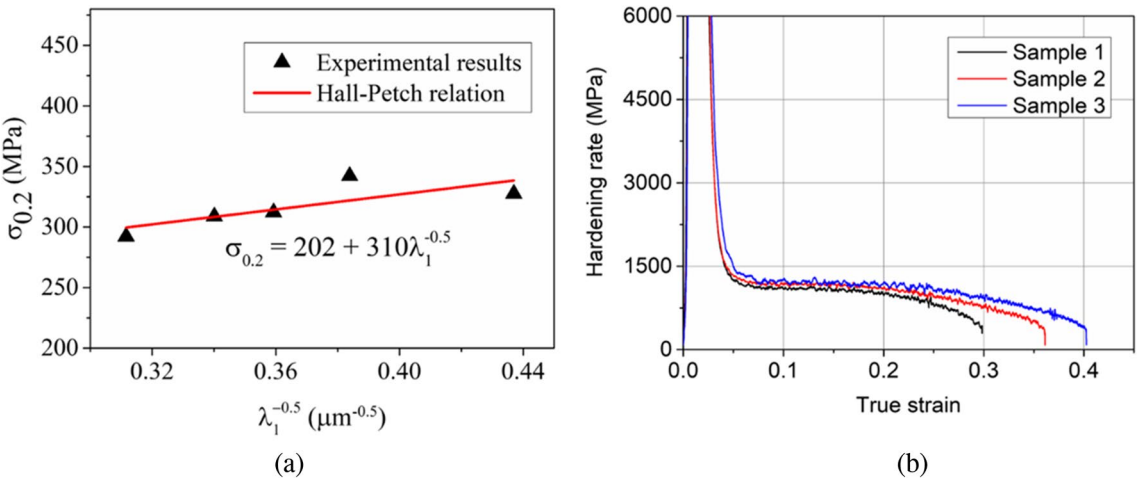

Fig. 16 Hall–Petch relationship between λ_1 (primary dendrite arm spacing) and yield stress (**a**), and the hardening rate-true train plot of samples 1, 2, and 3 (**b**)

and controlling microstructure and mechanical properties by a precise closed-loop control of measurable thermal signals in DED.

6 Conclusion

In this study, five AISI 316L thin-wall samples were deposited by DED with the in situ monitoring of thermal behaviors using a paraxial IR camera. The effects of the measured temperature gradient and solidification rate on solidification microstructure and mechanical properties were studied. The main conclusions are addressed as follows:

(1) The emissivity at high temperature in the IR image was calibrated using the in situ measurement of the melt pool length, extracted from the coaxial visual module, and the emissivity increases with larger heat input. The true temperature distribution of the DED AISI 316L sample was restored. The evolution of the melting interface at the head of the melt pool and the solidification interface at the tail of the melt pool were distinguished. The melt pool collapsed at the edge due to different thermal condition and edge geometry were verified by the experimental measures.

(2) The temperature gradient G and solidification rate R were extracted from the online temperature distribution. The temperature gradient of the melt pool is a complex vector field and the numerical temperature gradient decreased with the increase of laser power. Solidification rate increased along the solidification interface and increase with higher scanning speed.

(3) The microstructure of DED AISI 316L consists of coarse columnar grains and equiaxed grains. CET occurred at the upper part of the layer and most of the equiaxed grains were melted when depositing the next layer. The modified microstructure map for DED AISI 316L was established to predict CET at the top of a layer. The continuous growth of columnar grains following the orientation of previous columnar grains was in situ distinguished by the monitored heat flux direction.

(4) The framework relationship, combining thermal behaviors, average primary arm spacing, and yield stress has been developed, which can provide an experimental and theoretical guide in control of microstructure and property of deposition layers by closed-loop control of measurable solidification parameters in DED process. This experimental relationship shows that decreasing laser power and increasing scanning speed will contribute to a small λ_1 due to the joint effect of numerical temperature gradient and solidification rate, and a finer λ_1 will lead to an increase of yield stress and Vickers hardness.

Appendix

Table 5 Main symbol table

Symbol	Representative significance	Unit
λ_1	Primary dendrite arm spacing	μm
G	Temperature gradient	K/m
R	Solidification rate	K/s
J_T	Heat flux	W/m^2
V	Welding speed	m/s
ε	Strain	-

Table 6 Abbreviation comparison table

Abbreviation	Full name
DED	Directed energy deposition
CMOS	Coaxial complementary metal oxide semiconductor
AM	Additive manufacturing
LMD	Laser melting deposition
PDAS	Primary dendrite arm spacing
CET	Columnar to equiaxed transition
SLM	Selective laser melting
EBSD	Electron back scattered diffraction
BD	Building direction
FOV	Field of view

Acknowledgements The authors would like to thank Zijue Tang and Zhaorui Yan for their valuable guidance on data analysis.

Funding This research work was supported by the National Natural Science Foundation of China (Nos. 52175455 and 51975100), the Liaoning Provincial Science and Technology Plan Project, and the Fundamental Research Funds for the Central Universities.

Data availability The datasets generated and supporting the findings of this article are obtainable from the corresponding author upon reasonable request.

Declarations

Competing interest The authors declare no competing interests.

References

1. Liu S, Shin YC (2019) Additive manufacturing of Ti6Al4V alloy: a review. Materials & Design 164:107552. https://doi.org/10.1016/j.matdes.2018.107552
2. Saboori A, Aversa A, Marchese G, Biamino S, Lombardi M, Fino P (2019) Application of directed energy deposition-based additive

manufacturing in repair. Appl Sci 9:16. https://doi.org/10.3390/app9163316
3. Tan C, Weng F, Sui S, Chew Y, Bi G (2021) Progress and perspectives in laser additive manufacturing of key aeroengine materials. Int J Mach Tools Manuf 170:103804. https://doi.org/10.1016/j.ijmachtools.2021.103804
4. Salmi M (2021) Additive manufacturing processes in medical applications. Materials (Basel) 14:1. https://doi.org/10.3390/ma14010191
5. Blakey-Milner B, Gradl P, Snedden G, Brooks M, Pitot J, Lopez E, Leary M, Berto F, du Plessis A (2021) Metal additive manufacturing in aerospace: a review. Materials & Design 209:110008. https://doi.org/10.1016/j.matdes.2021.110008
6. Chen B, Yao Y, Huang Y, Wang W, Tan C, Feng J (2019) Quality detection of laser additive manufacturing process based on coaxial vision monitoring. Sens Rev 39(4):512–521. https://doi.org/10.1108/sr-03-2018-0068
7. Zheng B, Haley JC, Yang N, Yee J, Terrassa KW, Zhou Y, Lavernia EJ, Schoenung JM (2019) On the evolution of microstructure and defect control in 316L SS components fabricated via directed energy deposition. Mater Sci Eng: A. 764:138243. https://doi.org/10.1016/j.msea.2019.138243
8. Hu Y, Chen H, Liang X, Xie J (2021) Monitoring molten pool temperature, grain size and molten pool plasma with integrated area of the spectrum during laser additive manufacturing. J Manuf Process 64:851–860. https://doi.org/10.1016/j.jmapro.2021.01.040
9. Hooper PA (2018) Melt pool temperature and cooling rates in laser powder bed fusion. Addit Manuf 22:548–559. https://doi.org/10.1016/j.addma.2018.05.032
10. Hossein Nedjad S, Yildiz M, Saboori A (2022) Solidification behaviour of austenitic stainless steels during welding and directed energy deposition. Sci Technol Weld Joining 28(1):1–17. https://doi.org/10.1080/13621718.2022.2115664
11. Farshidianfar MH, Khodabakhshi F, Khajepour A, Gerlich AP (2021) Closed-loop control of microstructure and mechanical properties in additive manufacturing by directed energy deposition. Mater Sci Eng: A. 803:140483. https://doi.org/10.1016/j.msea.2020.140483
12. Criales LE, Arısoy YM, Lane B, Moylan S, Donmez A, Özel T (2017) Laser powder bed fusion of nickel alloy 625: experimental investigations of effects of process parameters on melt pool size and shape with spatter analysis. Int J Mach Tools Manuf 121:22–36. https://doi.org/10.1016/j.ijmachtools.2017.03.004
13. Misra S, Mohanty I, Raza MS, Chakraborty R, Chatterjee P, Gopal M, Ponkshe S, Saha P, Kumar CS (2022) Investigation of IR pyrometer-captured thermal signatures and their role on microstructural evolution and properties of Inconel 625 tracks in DED-based additive manufacturing. Surf Coat Technol 447:128818. https://doi.org/10.1016/j.surfcoat.2022.128818
14. Kriczky DA, Irwin J, Reutzel EW, Michaleris P, Nassar AR, Craig J (2015) 3D spatial reconstruction of thermal characteristics in directed energy deposition through optical thermal imaging. J Mater Process Technol 221:172–186. https://doi.org/10.1016/j.jmatprotec.2015.02.021
15. Altenburg SJ, Scheuschner N, Straße A, Gumenyuk A, Maierhofer C, Zalameda JN, Mendioroz A. (2021) Towards the determination of real process temperatures in the LMD process by multispectral thermography. Thermosense: thermal infrared applications XLIII 11743:117430B. https://doi.org/10.1117/12.2587881
16. Farshidianfar MH, Khajepour A, Gerlich AP (2016) Effect of real-time cooling rate on microstructure in laser additive manufacturing. J Mater Process Technol 231:468–478. https://doi.org/10.1016/j.jmatprotec.2016.01.017
17. Marshall GJ, Young WJ, Thompson SM, Shamsaei N, Daniewicz SR, Shao S (2016) Understanding the microstructure formation of Ti-6Al-4V during direct laser deposition via in-situ thermal monitoring. Jom 68(3):778–790. https://doi.org/10.1007/s11837-015-1767-z
18. Doubenskaia M, Pavlov M, Grigoriev S, Smurov I (2013) Definition of brightness temperature and restoration of true temperature in laser cladding using infrared camera. Surf Coat Technol 220:244–247. https://doi.org/10.1016/j.surfcoat.2012.10.044
19. Devesse W, De Baere D, Hinderdael M, Guillaume P (2016) High resolution temperature estimation during laser cladding of stainless steel. Phys Procedia 83:1253–1260. https://doi.org/10.1016/j.phpro.2016.08.132
20. Yang K, Wang ZD, Chen MZ, Lan HF, Sun GF, Ni ZH (2021) Effect of pulse frequency on the morphology, microstructure, and corrosion resistance of high-nitrogen steel prepared by laser directed energy deposition. Surf Coat Technol 421:127450. https://doi.org/10.1016/j.surfcoat.2021.127450
21. Saboori A, Aversa A, Bosio F, Bassini E, Librera E, De Chirico M, Biamino S, Ugues D, Fino P, Lombardi M (2019) An investigation on the effect of powder recycling on the microstructure and mechanical properties of AISI 316L produced by directed energy deposition. Mater Sci Eng: A 766:138360. https://doi.org/10.1016/j.msea.2019.138360
22. Akbari M, Kovacevic R (2018) An investigation on mechanical and microstructural properties of 316LSi parts fabricated by a robotized laser/wire direct metal deposition system. Addit Manuf 23:487–497. https://doi.org/10.1016/j.addma.2018.08.031
23. Moheimani SK, Iuliano L, Saboori A (2022) The role of substrate preheating on the microstructure, roughness, and mechanical performance of AISI 316L produced by directed energy deposition additive manufacturing. Int J Adv Manuf Technol 119(11–12):7159–7174. https://doi.org/10.1007/s00170-021-08564-4
24. Roehling TT, Wu SSQ, Khairallah SA, Roehling JD, Soezeri SS, Crumb MF, Matthews MJ (2017) Modulating laser intensity profile ellipticity for microstructural control during metal additive manufacturing. Acta Mater 128:197–206. https://doi.org/10.1016/j.actamat.2017.02.025
25. Terrassa KL, Smith TR, Jiang S, Sugar JD, Schoenung JM (2019) Improving build quality in directed energy deposition by cross-hatching. Mater Sci Eng: A 765:138269. https://doi.org/10.1016/j.msea.2019.138269
26. DebRoy T, Wei HL, Zuback JS, Mukherjee T, Elmer JW, Milewski JO, Beese AM, Wilson-Heid A, De A, Zhang W (2018) Additive manufacturing of metallic components – process, structure and properties. Prog Mater Sci 92:112–224. https://doi.org/10.1016/j.pmatsci.2017.10.001
27. Liu Z, Zhao D, Wang P, Yan M, Yang C, Chen Z, Lu J, Lu Z (2022) Additive manufacturing of metals: microstructure evolution and multistage control. J Mater Sci Technol 100:224–236. https://doi.org/10.1016/j.jmst.2021.06.011
28. Liu Y, Shi J (2023) Epitaxial growth and stray grain control toward single-crystal metallic materials by additive manufacturing: a review. Adv Eng Mater. https://doi.org/10.1002/adem.202201917
29. Kurz W, Fisher DJ (1981) Dendrite growth at the limit of stability - tip radius and spacing. Acta Metall 29(1):11–20. https://doi.org/10.1016/0001-6160(81)90082-1
30. Huang Y, Ansari M, Asgari H, Farshidianfar MH, Sarker D, Khamesee MB, Toyserkani E (2019) Rapid prediction of real-time thermal characteristics, solidification parameters and microstructure in laser directed energy deposition (powder-fed additive manufacturing). J Mater Process Technol 274:116286. https://doi.org/10.1016/j.jmatprotec.2019.116286

31. Raghavan N, Simunovic S, Dehoff R, Plotkowski A, Turner J, Kirka M, Babu S (2017) Localized melt-scan strategy for site specific control of grain size and primary dendrite arm spacing in electron beam additive manufacturing. Acta Mater 140:375–387. https://doi.org/10.1016/j.actamat.2017.08.038
32. Scipioni Bertoli U, MacDonald BE, Schoenung JM (2019) Stability of cellular microstructure in laser powder bed fusion of 316L stainless steel. Mater Sci Eng, A 739:109–117. https://doi.org/10.1016/j.msea.2018.10.051
33. Gaumann M, Bezencon C, Canalis P, Kurz W (2001) Single-crystal laser deposition of superalloys: processing-microstructure maps. Acta Mater 49(6):1051–1062. https://doi.org/10.1016/S1359-6454(00)00367-0
34. Ren YM, Lin X, Fu X, Tan H, Chen J, Huang WD (2017) Microstructure and deformation behavior of Ti-6Al-4V alloy by high-power laser solid forming. Acta Mater 132:82–95. https://doi.org/10.1016/j.actamat.2017.04.026
35. Yin J, Peng GY, Chen CP, Yang JJ, Zhu HH, Ke LD, Wang ZM, Wang DZ, Ma MM, Wang GQ, Zeng XY (2018) Thermal behavior and grain growth orientation during selective laser melting of Ti-6Al-4V alloy. J Mater Process Technol 260:57–65. https://doi.org/10.1016/j.jmatprotec.2018.04.035
36. Shi DH, Zou FH, Zhu ZL, Sun JF (2015) Modeling the effect of surface oxidation on the normal spectral emissivity of steel 316L at 1.5 μm over the temperatures ranging from 800 to 1100 K in air. Infrared Phys Technol 71:370–377. https://doi.org/10.1016/j.infrared.2015.05.012
37. Blecher JJ, Palmer TA, DebRoy T (2014) Solidification map of a nickel-base alloy. Metall Mater Trans a-Phys Metall Mater Sci 45(4):2142–51. https://doi.org/10.1007/s11661-013-2149-1
38. Hussein A, Hao L, Yan CZ, Everson R (2013) Finite element simulation of the temperature and stress fields in single layers built without-support in selective laser melting. Mater Des 52:638–647. https://doi.org/10.1016/j.matdes.2013.05.070
39. Bi G, Sun CN, Gasser A (2013) Study on influential factors for process monitoring and control in laser aided additive manufacturing. J Mater Process Technol 213(3):463–468. https://doi.org/10.1016/j.jmatprotec.2012.10.006
40. Fan ZQ, Zhao YT, Tan QY, Mo N, Zhang MX, Lu MY, Huang H (2019) Nanostructured Al2O3-YAG-ZrO2 ternary eutectic components prepared by laser engineered net shaping. Acta Mater 170:24–37. https://doi.org/10.1016/j.actamat.2019.03.020
41. Muvvala G, Patra Karmakar D, Nath AK (2017) Online monitoring of thermo-cycles and its correlation with microstructure in laser cladding of nickel based super alloy. Opt Lasers Eng 88:139–152. https://doi.org/10.1016/j.optlaseng.2016.08.005
42. Jiang W, Chen X, Wang B, Fan Z, Wu H (2016) Effects of vibration frequency on microstructure, mechanical properties, and fracture behavior of A356 aluminum alloy obtained by expendable pattern shell casting. Int J Adv Manuf Technol 83(1–4):167–175. https://doi.org/10.1007/s00170-015-7586-0
43. Lin X, Li YM, Wang M, Feng LP, Chen J, Huang WD (2003) Columnar to equiaxed transition during alloy solidification. Sci China Ser E-Technol Sci 46(5):475–489. https://doi.org/10.1360/02ye0337
44. Singh KK, Sangal S, Murty GS (2002) Hall-Petch behaviour of 316L austenitic stainless steel at room temperature. Mater Sci Technol 18(2):165–172. https://doi.org/10.1179/026708301125000384
45. Kashyap BP, Tangri K (1997) Hall-Petch relationship and substructural evolution in boron containing type 316L stainless steel. Acta Mater 45(6):2383–2395. https://doi.org/10.1016/S1359-6454(96)00341-2